RSC Advances

PAPER

View Article Online
View Journal | View Issue

Cite this: *RSC Adv.*, 2026, **16**, 25705

Designable NIR-II light triggered biocompatible Au NRs for highly efficient photothermal therapy of cervical cancer

Jiabao Xiong,†[ab] Hairegu Tuxun,†[ac] Jiayi Ding,[d] Biao Dong *[e] and Nuernisha Alifu *[abc]

Gold nanorods (Au NRs) hold great potential for photothermal therapy (PTT) of cervical cancer, but their clinical application is hindered by suboptimal absorbance in the second near-infrared (900–1700 nm, NIR-II) spectral window, synthetic heterogeneity, and cytotoxic surfactant residues. To overcome these limitations, we combined computational design with experimental synthesis and developed novel type of NIR-II-optimized Au NRs. Finite-difference time-domain simulations predicted that Au NRs exhibited 88 nm of length and 13 nm of diameter with a strong localized surface plasmon resonance (LSPR) peak at 1058 nm, enabling deep tissue penetration in the NIR-II spectral region. Experimentally, we synthesized highly uniform Au NRs@PEG nanoparticles (NPs) *via* a seed-growth method, achieving a 1026 nm absorption peak while replacing toxic cetyltrimethylammonium bromide (CTAB) with biocompatible polyethylene glycol (SH-PEG-5000). The Au NRs@PEG demonstrated exceptional photothermal conversion efficiency of 60.89%, excellent tumor accumulation, and minimal systemic toxicity. *In vivo* studies confirm effective tumor suppression of 93.5% under NIR-II light excitation, with the stability for repeated treatment cycles. In this work, we introduce a versatile paradigm for designing high-performance, clinically viable photothermal agents by means of rational optical engineering and surface modification.

Received 31st December 2025
Accepted 26th March 2026

DOI: 10.1039/d5ra10095j

rsc.li/rsc-advances

Introduction

Cervical cancer is one of the most prevalent cancers affecting women worldwide.[1,2] Traditional treatment methods, including surgical resection,[3] radiotherapy,[4] and chemotherapy,[5] are commonly used in the management of cervical cancer. However, each of these approaches has inherent limitations. Surgical resection often faces challenges in achieving complete tumor removal, and it can also lead to complications, such as tissue trauma and negative impacts on future fertility.[6] Radiotherapy, which uses high-energy X-rays or γ radiation, can cause irreversible damage to both cancerous and normal cells.[7,8] Chemotherapy, although effective, lacks specificity for cancer cells, leading to collateral damage to healthy tissues.[9] To overcome these limitations, considerable research efforts have been dedicated to developing innovative diagnostic and therapeutic strategies.[10–13] Among these, photothermal therapy (PTT) based on nanomaterials has been considered a promising therapeutic approach. The main reasons include short treatment time (about a few minutes), minimal evasiveness, significant therapeutic effects, and fewer side effects (most photosensitizers are relatively harmless at low concentrations).[14,15]

In particular, PTT in the second near-infrared (900–1700 nm, NIR-II) spectral window has gained significant attention due to its deep-tissue penetration capability (>5 mm) and low phototoxicity.[16,17] Gold nanomaterials, which are currently favorable for clinical trials,[18] have played a key role in this development. Since the discovery of the photothermal effect, gold nanorods (Au NRs) have been extensively studied for PTT due to their tunable local surface plasmon resonance (LSPR) properties.[19] Au NRs, with their unique anisotropic structure, allow precise tuning of their LSPR absorption peak from the visible and the NIR wavelength regions (650–1300 nm) by adjusting the aspect ratio. This ability makes them one of the most important materials for PTT, as well as the noble metal nanomaterials with the most easily adjustable optical properties. The therapeutic efficacy of Au NRs is closely related with their LSPR wavelength, particle uniformity, and biocompatibility.[20–22] However, current

[a]*State Key Laboratory of Pathogenesis, Prevention and Treatment of High Incidence Diseases in Central Asia/School of Medical Engineering and Technology, Xinjiang Medical University, Urumqi 830054, China. E-mail: nens_xjmu@126.com*

[b]*The Second Affiliated Hospital of Xinjiang Medical University, Xinjiang Medical University, Urumqi 830054, China*

[c]*Institute of Medical Engineering Interdisciplinary Research, Xinjiang Medical University, Urumqi, 830017, China*

[d]*School of Public Health, Xinjiang Medical University, Urumqi 830054, China*

[e]*College of Electronic Science and Engineering, Jilin University, Changchun 130012, China. E-mail: dongb@jlu.edu.cn*

† Jiabao Xiong and Hairegu Tuxun contributed equally to this work.

Au NRs often face challenges such as size and shape heterogeneity, absorption peaks that are limited to the shorter NIR spectral region (*e.g.*, 808 nm), and the use of toxic surfactants, like cetyltrimethylammonium bromide (CTAB). Furthermore, non-uniform nanoparticles (NPs) tend to aggregate *in vivo* nonspecifically, increasing the risk of biological toxicity. Residual reagents may also damage cell membranes and provoke inflammatory responses, severely hindering their clinical translation.[23]

Recent advances have led to the development of Au NRs-based nanoplatforms that improve their biocompatibility and therapeutic efficiency. These include simple chemical modifications with organic materials and polymers, such as polyethylene glycol (PEG). For instance, Chen *et al.* developed an Au NRs@DOX drug delivery system that achieved photothermal effects under 808 nm NIR light, resulting in increased apoptosis of the tumor cells, and improved therapeutic outcomes both *in vitro* and *in vivo*.[24] Moreover, Au NRs vesicles coated with PEG show improved photothermal conversion efficiency (PCE) and optical responsiveness, suggesting potential for future imaging applications.[25]

This study uses a size-dependent refractive index model and finite-difference time-domain (FDTD) simulation software to analyze the optical absorption properties of Au NRs. The simulation results indicated that Au NRs with a length of 88 nm and a diameter of 13 nm exhibited a pronounced longitudinal localized surface plasmon resonance (L-LSPR) absorption peak at 1058 nm. Based on these insights, a high-uniformity Au NR system with NIR-II absorption characteristics (1026 nm) was prepared using a seed growth method. SH-PEG modification was used to replace the traditional CTAB surfactant, thereby eliminating surface toxicity residues. This study explores the potential of PEG-coated gold nanorods (Au NRs@PEG) as photothermal agents under NIR-II light irradiation. The results demonstrate that Au NRs@PEG nanoparticles (NPs) effectively suppress cervical tumor growth. PCE and toxicity tests showed that Au NRs@PEG accumulate in the liver and spleen, localizing around tumor cells. *In vivo* studies confirmed the photothermal stability of Au NRs, supporting multiple treatment sessions after a single injection. The material exhibited high PCE, causing substantial temperature elevation under low-light conditions and effective tumor growth inhibition, substantiating its potential for tumor treatment.

Materials and methods

Materials

Without undergoing additional purification, all chemicals were used directly upon receipt, and deionized water was applied in all experimental procedures. Sinopharm Chemical Reagent Co., Ltd. (Shanghai, China) made available hydrochloric acid (HCl), sodium hydroxide (NaOH), ascorbic acid, and glycine, while Sigma Aldrich (Shanghai, China) supplied the sodium borohydride ($NaBH_4$), cetyltrimethylammonium bromide (CTAB), gold(III) chloride hydrate ($HAuCl_4$), silver nitrate ($AgNO_3$), Indocyanine Green (ICG) and sodium oleate (NaOL) utilized in the experiments. Gibco (Shanghai, China) made available Dulbecco's modified Eagle's medium (DMEM), penicillin-streptomycin, phosphate-buffered saline (PBS), and 0.25% trypsin containing EDTA for the experiments. Bis-benzamide H33342 (4,6-diamidino-2-phenylindole), and dimethyl sulfoxide were provided by Thermo Fisher Scientific Co., Ltd. The Calreticulin (CRT) Rabbit Monoclonal Antibody, High Mobility Group Box 1 (HMGB1) Rabbit Monoclonal Antibody, and Mitochondrial Membrane Potential Assay Kit with JC-1 were sourced from Beyotime (Shanghai, China). Furthermore, 4% paraformaldehyde, hematoxylin–eosin, EDTA-anticoagulation tubes, cell counting kit-8 (CCK-8), sourced from the china-based Weierbo Biotechnology Co., Ltd., were utilized in the experiments.

Characterization

Au NRs and Au NRs@PEG were characterized through UV-vis spectroscopy, zeta-potential measurements, FT-IR spectroscopy, and a transmission electron microscope (TEM) (JEOL JEM1230, Japan) run at 200 kV accelerating voltage. The intracellular internalization behavior of Au NRs and Au NRs@PEG was investigated with a Nikon ECLIPSE Ti confocal laser scanning microscope (CLSM, Japan), and a thermal imaging device from Heat Image Technology Co., Ltd. (Shanghai, China) was used for temperature monitoring. The assessment of cell viability was conducted utilising a microplate reader (Thermo Fisher, USA). Flow cytometry experiments were implemented with a BD FACS Canto flow cytometer (BD Biosciences, USA), alongside routine blood examinations and hepatic-renal function tests performed on a Mindray BS-240 VET. The optical imaging investigations involved conducting ex vivo and *in vivo* NIR-I fluorescence imaging spectra using a PerkinElmer IVIS Spectrum small-animal imaging system.

Synthesis of Au NRs

Au NRs were fabricated by means of a binary surfactant method,[26] and the synthesis of these nanomaterials comprises two key steps as follows:

Seed preparation. 0.01 M of $HAuCl_4$ solution (0.125 mL) was introduced into 4.75 mL of CTAB (0.1 M) aqueous dispersion in a plastic tube. To blend the solutions, the mixture was gently inverted, and 0.3 mL of ice-chilled freshly prepared $NaBH_4$ (0.01 M) was added all at once. The solution underwent rapid inversion for 2 minutes and was then left to stand without disturbance for 2 hours.

Growth process. In a plastic tube containing 10 mL of CTAB (10 mM) aqueous solution, 0.5 mL of $HAuCl_4$ (10 mM) and 80 μL of $AgNO_3$ (10 mM) were sequentially incorporated for each aliquot. Gentle inversion was conducted to mix the components, followed by adding 80 μL of freshly formulated 100 mM L-ascorbic acid solution and subsequent thorough mixing. Aliquots of the growth solution were supplemented with different volumes of CTAB-stabilized seed solution, and each reaction mixture was gently agitated for 10 seconds before being left to rest without disturbance overnight.

Preparation of Au NRs@PEG. The as-prepared Au NR suspension was centrifuged, and the collected NRs were

redispersed into 10 mL of aqueous medium. Subsequently, 0.5 mL of thiol-poly (ethylene glycol)-5000 (CH_3O-PEG-SH) with a concentration of 0.05 g/10 mL was added, followed by allowing the mixture to stand undisturbed overnight. For the synthesis of ICG-loaded Au NRs@PEG, simply add both ICG and SH-PEG-5000 simultaneously, and allow the mixture to stir overnight in the dark.

Cell culture and cellular uptake

HeLa human cervical adenocarcinoma cells were procured from the American Type Culture Collection (ATCC, Manassas, VA, USA) and cultured in a complete growth medium consisting of 45 mL of high-glucose DMEM (90%), 4 mL of 8% fetal bovine serum, and 0.5 mL of a dual-antibiotic solution was dispensed as per typical cell culture protocols. HeLa cells were cultivated in an incubator maintained at 37 °C, with a carbon dioxide concentration of 5%. CLSM was employed to analyze HeLa cells exposed to varying concentrations (40, 80, and 100 μg mL^{-1}) of treatment, each in a volume of 600 μL. The cells were seeded into 35 mm glass-bottomed dishes at a density of 1×10^5 cells per well and incubated overnight.

Cytotoxicity analysis

The cytotoxic effect of Au NRs@PEG was evaluated using a CCK-8 assay. 96-well culture plates were seeded with HeLa cells at 3×10^3 cells per well, and the plates were incubated overnight. Thereafter, the cells were exposed to Au NRs@PEG at different dosage levels (10, 20, 30, 40, 60, 80, 100, and 120 μg mL^{-1}), in conjunction with control and blank groups, for 4 hours of incubation. After this incubation step, the wells underwent 10 minutes of exposure to a 1064 nm laser (400 mW cm^{-2}). Once laser treatment was finished, each well received 10 μL of CCK-8 reagent, with the plates then subjected to incubation in darkness for 2 hours. Cell viability was calculated using eqn (1) below:

$$\text{Cell viability } (\%) = \frac{OD_{sample} - OD_{blank}}{OD_{negative} - OD_{blank}} \times 100\% \quad (1)$$

the optical density (OD) of cells treated with Au NRs@PEG is represented by OD_{sample}, the OD of the PBS medium without cells is referred to as OD_{blank}, and the OD of the medium containing cells is denoted as $OD_{negative}$. The measurement of OD at 450 nm was facilitated by a microplate reader.

In vitro cell apoptosis assay

HeLa cells were plated onto confocal dishes, cultured for 24 hours, and then treated with Au NRs@PEG for an additional 6 hours. Following the incubation period, the cells were exposed to 1064 nm NIR irradiation at a power of 400 mW cm^{-2} for a duration of 10 minutes. Subsequent to the exposure, the cells were subjected to an incubation at 37 °C for a duration of 20 minutes, in the presence of a mixture comprising Calcein-AM at a concentration of 2 μM and propidium iodide (PI) at a concentration of 5 μM. The cells were washed with PBS and imaged using a CLSM. To investigate the cell death mechanism in greater detail, we employed a flow cytometry technique, utilizing an Annexin V-FITC/PI apoptosis detection kit. Subsequent to the treatment, the cells were incubated with Annexin V-FITC and PI for a period of 10 minutes at room temperature. Thereafter, analysis was conducted using flow cytometry.

Photothermal analysis *in vitro*

This study set out with the aim of establishing a relationship between photothermal efficiency and suspension concentration, as well as laser power intensity. To achieve this, 0.5 mL of Au NRs@PEG dispersions in water, with concentrations of 12.5, 25, and 50 μg mL^{-1}, were exposed to a 1064 nm laser at power densities of 100, 300, 400, and 500 mW cm^{-2}. An infrared thermal imaging system was employed to monitor temperature fluctuations from the initial temperature to the maximum and most stable temperature attained. The monitoring was performed at 30 second intervals for a period of 10 minutes to ascertain the optimal laser power density. Subsequent assessment of the PCE (η) of Au NRs@PEG was conducted by subjecting a 25 μg mL^{-1} aqueous dispersion to a 1064 nm laser at an intensity of 400 mW cm^{-2}. Subsequent to the attainment of thermal equilibrium by the solution, the laser was deactivated, thereby facilitating a reversion of the temperature to ambient conditions. During this process, thermal imaging facilitated the documentation of temperature dynamics. The η can be calculated using eqn (2):

$$\eta\ (\%) = \frac{hS(T_{max} - T_{surr})}{I\left(1 - 10^{-A_{1064}}\right)} \times 100\% \quad (2)$$

where h denotes the heat transfer coefficient, S corresponds to the surface area of the reaction vessel, and I stands for the laser power, T_{max} is the peak temperature achieved, T_{surr} is the surrounding temperature, and A_{1064} stands for the absorbance of the sample at 1064 nm. The value of hS may be determined *via* eqn (3):

$$hS = \frac{M_D C_D}{\tau_s} \quad (3)$$

where M_D (solvent mass) was 0.5 mg, and C_D (solvent heat capacity) was 4.2 J g^{-1} $°C^{-1}$. τ_s is a constant specific to the sample system, calculated using eqn (4)

$$\tau_s = -\ln\left(\frac{T_t - T_{surr}}{T_{max} - T_{surr}}\right) \quad (4)$$

Cell scratch assay

HeLa cells were plated in a six-well cell culture plate and allowed to reach confluence. Following this, a scratch wound model was established by vertically pressing a 200 μL pipette tip against the monolayer of cells, creating a straight scratch line. Subsequently, the wound area was periodically imaged at intervals of several hours. In addition, 3–5 random sites were selected carefully, and the degree of cell migration was evaluated through measurement of the distance changes between the wound edges over time. The final data were then analyzed using ImageJ software.

Assessment of mitochondrial membrane potential

Following the established culture and treatment protocols, cells were washed once with PBS after treatment and then incubated with 1 mL of JC-1 staining working solution at 37 °C in the dark for 20 minutes. After three washes with PBS, mitochondrial membrane potential was evaluated using CLSM.

Evaluation of CRT exposure and HMGB1 migration

HeLa cells were cultured and treated according to the established protocols. After treatment, cells were washed three times with PBS, followed by the addition of CRT and HMGB1 antibody solutions, and incubated at 4 °C for 24 hours. After removing the antibodies and washing the cells three times with PBS, fluorescently labeled secondary antibodies were added and incubated at room temperature for 2 hours. Following the removal of the secondary antibodies, cells were washed three times with PBS. Finally, fluorescence images were captured using a laser scanning confocal microscope.

NIR-I fluorescence imaging

ICG-loaded Au NRs@PEG (40 μg mL^{-1}) was intravenously injected into 15–18 g, six-to-eight-week-old female mice to assess the *in vivo* biodistribution of the nanoparticles. *In vivo* NIR fluorescence imaging was performed at 5 minutes, 1 hour, 2 hours, 4 hours, 8 hours, 12 hours, 24 hours, and 48 hours post-injection. Following this, the mice were euthanized, and major organs (heart, liver, spleen, lungs, kidneys) were harvested for *ex vivo* fluorescence imaging with excitation at 745 nm and emission at 840 nm.

Mouse model and *in vivo* antitumor study

A female BALB/c mouse model (6–8 weeks old) bearing HeLa tumors was established by injecting 1×10^6 HeLa cells (suspended in 100 μL of DMEM) into the axillary region. Once the tumor volume reached approximately 50 mm^3, the mice were randomly assigned to four groups of five: a control group (saline injection), a laser group (1064 nm laser treatment), an Au NRs@PEG group (Au NRs@PEG injection), and a combination group (Au NRs@PEG injection and 1064 nm laser treatment). The Au NRs@PEG dosage was 5 mg kg^{-1}. Mice in the relevant groups underwent NIR irradiation at 1064 nm with a power density of 400 mW cm^{-2} for 10 minutes. Temperature changes were monitored by infrared imaging. Tumor volume and body weight were measured at the tumor site every two days. Tumor volume was calculated using the formula: $V = (L \times W^2)/2$, where L is the maximum tumor length and W is the shortest transverse width. On day 14, the mice were euthanized, and tumors and vital organs were harvested for histological analysis with hematoxylin and eosin (H&E) staining.

Results and discussion

As illustrated in Scheme 1, Au NRs with strong absorption in the NIR-II window were synthesized *via* a seed-mediated growth method. Surface functionalization with SH-PEG-5000 was then performed to enhance biocompatibility. Effective photothermal ablation of cervical cancer cells was achieved using 1064 nm NIR-II laser irradiation, which provides deep tissue penetration.

Design of light absorption spectra of Au NRs

The optical properties of non-spherical NPs can be simulated by means of numerical methods, including the finite element method (FEM), the FDTD method, the discrete dipole

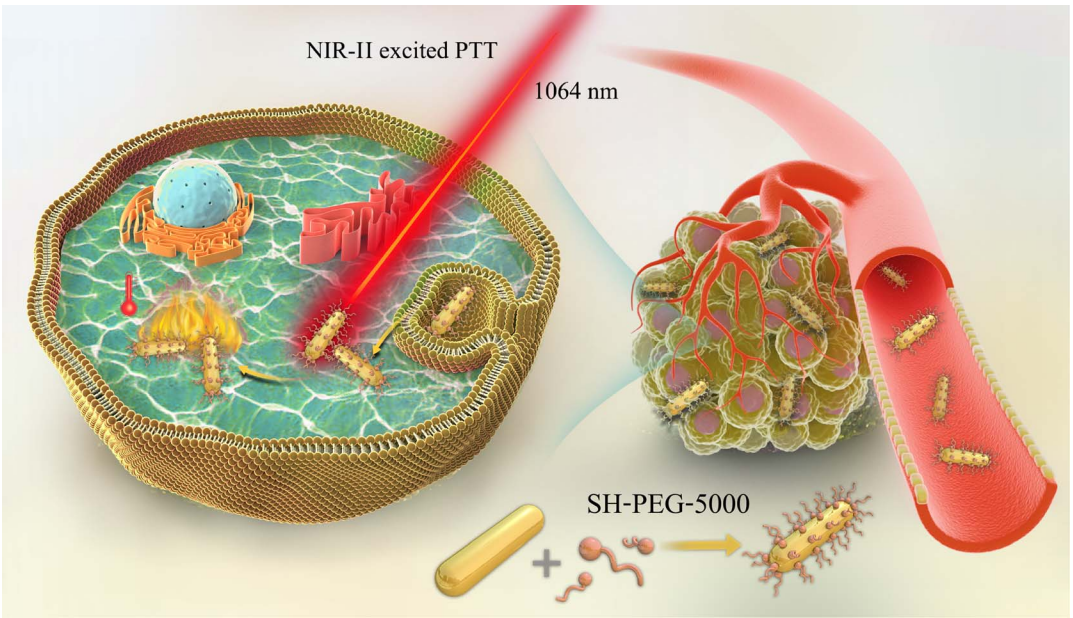

Scheme 1 Preparation of Au NRs@PEG and their application in NIR-II laser-assisted PTT of HeLa cells.

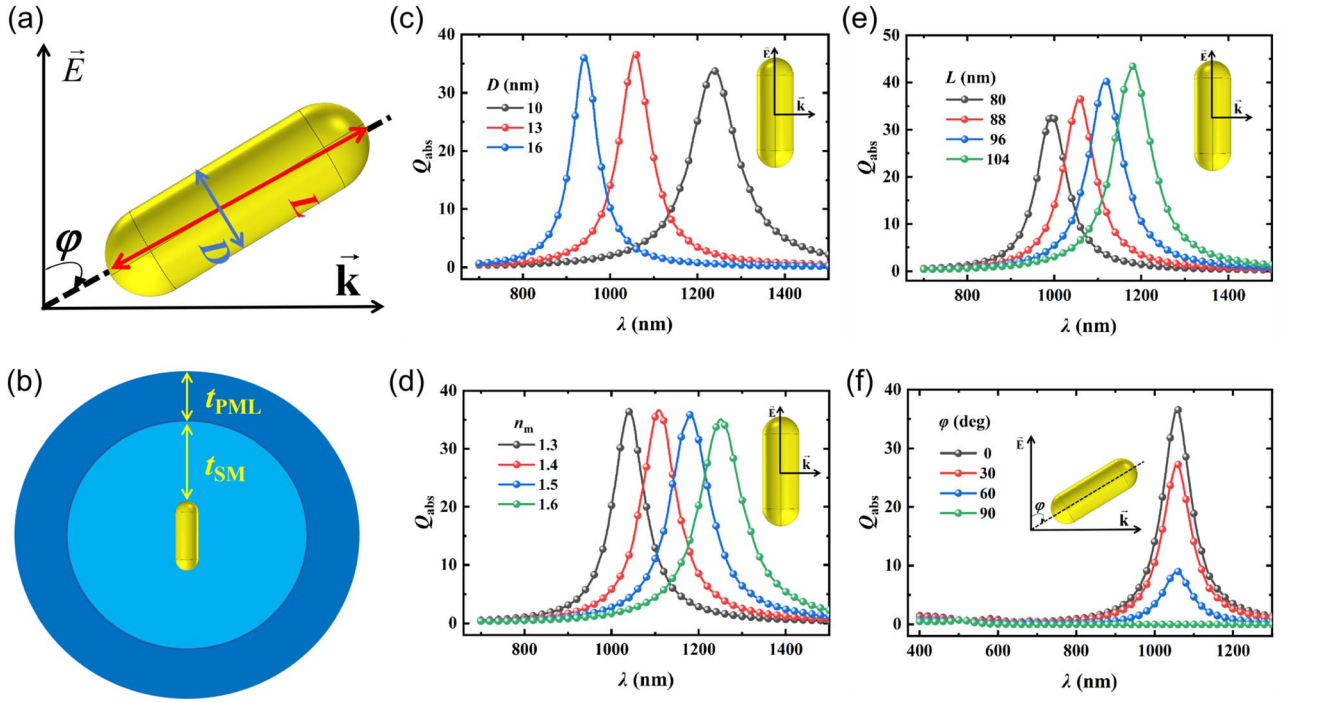

Fig. 1 Theoretical analysis of the optical characteristics of Au NRs. (a) Schematic illustration of the geometry and orientation of Au NRs. (b) FEM simulation configuration. (c) Variations in the absorbance spectra of Au NRs dispersed in water *versus* length *L*, with a diameter *D* of 13 nm and an angle φ set to 0°. (d) Changes in the absorbance profiles of Au NRs in aqueous solution dependent on diameter *D*, maintaining length $L = 88$ nm and angle $\varphi = 0°$. (e) Au NR absorbance spectra variations in water as a function of the refractive index (n_m) of biological tissue, with $L = 88$ nm, $D = 13$ nm, and $\varphi = 0°$. (f) Absorbance spectra changes of Au NRs in aqueous dispersion based on their orientation, with length $L = 88$ nm and diameter $D = 13$ nm.

approximation (DDA) and the boundary element method (BEM).[26–29] In this study, the light absorption properties of Au NRs were simulated using FEM with a size-dependent refractive index model. The nanorod consists of two hemispheres of diameter *D* and a cylinder with height $(L - D)$, as shown in Fig. 1a. This structural configuration has been demonstrated to exhibit enhanced compatibility with the morphology of the synthesised nanorods, thereby rendering it more amenable for practical processing and fabrication in a range of applications. Pursuant to the calculation, the following assumptions are made: the incident light propagates along the *x*-axis, the electric field oscillates along the *z*-axis, the rotation axis of the nanorod lies in the *xoz* plane, and φ is the angle between the rotation axis and the *z*-axis (*i.e.*, the azimuth). As demonstrated in Fig. 1b, a spherical region with a minimum thickness t_{SM} of 1/2 wavelength is designated as the surrounding medium (SM) layer external to the particle. A spherical region with a thickness equivalent to 1/4 of the wavelength of the TM layer is designated as a perfectly matched layer (PML) in the exterior region. The PML constitutes an artificial absorbing layer that truncates computational regions in numerical methods employed to simulate problems with open boundaries. The waves are completely absorbed in the PML in order to prevent them from returning as reflections.

The light absorption capacity of an individual nanoparticle can be quantitatively described by the absorption efficiency Q_{abs}, which can be expressed as eqn (5):[30]

$$Q_{abs} = \frac{1}{\pi R_{eff}{}^2 I_i} \iiint_{V_p} Q_h \, dV, \quad R_{eff} = \sqrt[3]{\frac{3V_p}{4\pi}} \tag{5}$$

in this context, Q_h corresponds to the optical power per unit area absorbed by the nanoparticle, V_p denotes the particle volume, and R_{eff} stands for the effective radius of the particle—equivalent to the radius of a sphere with equal volume. The intensity of the incident light is defined as $I_i = (n_m E_0{}^2)/(2Z_0)$, in which n_m denotes the refractive index of the SM, E_0 corresponds to the amplitude of the incident electric field (with a value fixed at 1 in the simulation), and Z_0 refers to the vacuum impedance. For NPs, acquiring the refractive index of the nanomaterials themselves is critical to determining their absorption efficiency (Q_{abs}). For metallic NPs, the refractive index depends on both the frequency of the incident light and the nanoparticle dimensions. This size dependence stems from the fact that when the nanoparticle size is less than the mean free path of free electrons, collisions between free electrons and the nanoparticle surface are enhanced, rendering surface scattering significant.[30] Thus, the size-dependent refractive index of metallic NPs can be formulated as follows:

$$n_{nano}(\omega, L_{eff}) = \sqrt{n_{bulk}{}^2(\omega) + \frac{\omega_p{}^2}{\omega^2 + \frac{i\omega v_f}{l_\infty}} - \frac{\omega_p{}^2}{\omega^2 + i\omega\left(\frac{v_f}{l_\infty} + \frac{A v_f}{L_{eff}}\right)}} \tag{6}$$

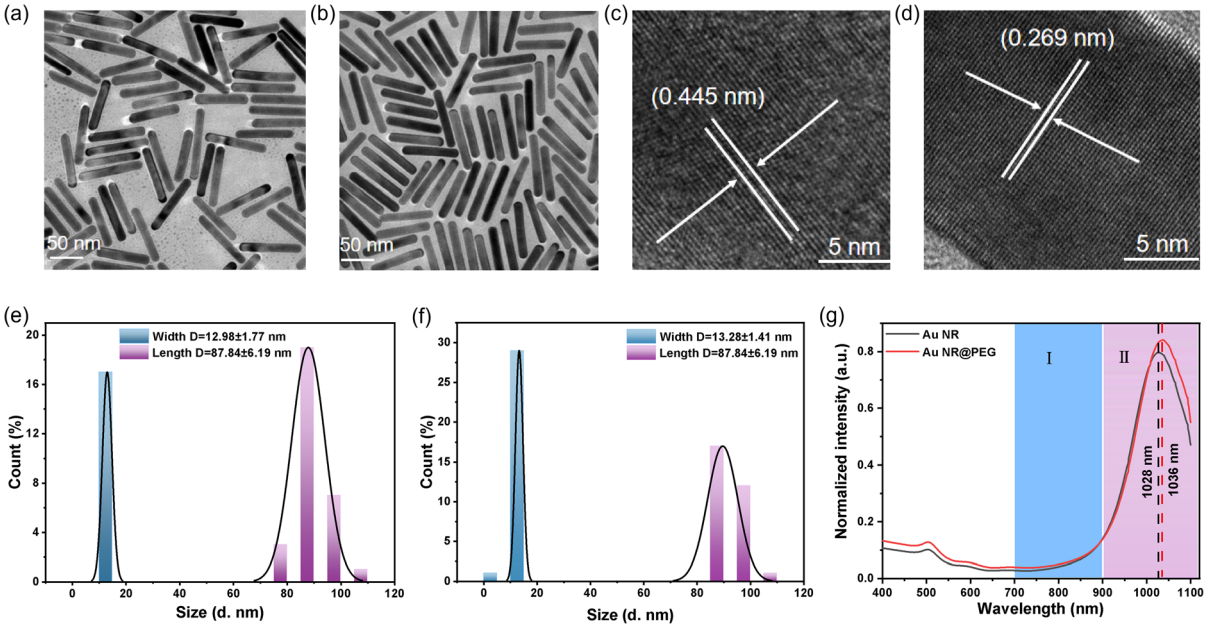

Fig. 2 Characterization of bare Au NRs and Au NRs@PEG. TEM micrographs of (a) bare Au NRs and (b) Au NRs@PEG are presented. (c) and (d) correspond to the lattice fringes of (a) and (b), respectively. Histograms of (e) bare Au NRs and (f) Au NRs@PEG illustrate the length and width distributions. Fifty NPs per sample were analyzed to quantify the length and width of bare Au NRs and Au NRs@PEG. (g) UV-vis-NIR absorbance spectra of bare Au NRs and Au NRs@PEG.

the angular frequency of the incident light (ω), the complex refractive index of bulk metals (n_{bulk}), the plasma frequency (ω_p), the Fermi velocity (v_f), the mean free path of the free electrons (l_∞), and the dimensionless parameter A (which approaches 1 in this paper) are considered. The effective free electron means free path (L_{eff}), which is typically taken as $L_{eff} = R_{eff}$, is also a key component of the model. Au bulk is obtained from the data published by McPeak,[31] and the values of ω_p = 9.03 eV, $v_f = 1.4 \times 1706$ m s^{-1}, and $l_\infty = 42$ nm are obtained from published papers.[32,33] The refractive index of water is obtained from the data published by Kedenburg.[34] In order to quantitatively analyze the effect of size on the absorption spectra, the volume absorption efficiency of Au NRs with lengths of 80 nm, 88 nm, 96 nm, and 104 nm was calculated as a function of wavelength, as illustrated in Fig. 1c. As the length increases from 80 to 104 nm, the resonance wavelength of the Au NRs shifts from 994 to 1182 nm, and their absorption capacity increases. The absorption efficiency of Au NRs with diameters of 10 nm, 13 nm, and 16 nm was calculated as a function of wavelength, as demonstrated in Fig. 1d. As the diameter increases from 10 nm to 16 nm, the resonance wavelength of the Au NRs shifts from 1238 nm to 942 nm. This shift is attributed to changes in the optical properties and electronic structure of the NPs. Firstly, the LSPR frequency of NPs undergoes a change in accordance with increasing size, resulting in a concomitant change in light absorption. Secondly, the electronic density of states of NPs undergoes a change with size, which in turn affects their ability to absorb photons.[35] The simulation results indicate that the resonance wavelength of Au NRs with a length of 88 nm and a diameter of 13 nm is 1058 nm, which is close to the 1064 nm laser wavelength.

The absorption efficiency of Au NRs in different biological tissues (with refractive indices of 1.3, 1.4, 1.5, and 1.6) was calculated as a function of wavelength, as shown in Fig. 1e. As the refractive index of the biological tissue increases from 1.3 to 1.6, the resonance wavelength of the Au NRs redshifts from 1040 nm to 1250 nm, and the absorption efficiency decreases from 36.39 to 35.07. The underlying cause of this phenomenon is the increase in the refractive index of the SM, which results in a decrease in the speed of light propagation and a concomitant reduction in the wavelength of light within the medium. This results in an increase in the wavelength of the incident light that excites the LSPR of the NPs.

The absorption efficiency of Au NRs for four distinct orientations ($\varphi = 0°$, 30°, 60°, and 90°) was computed across a range of wavelengths, as depicted in Fig. 1f. Two separate resonance peaks were identified in the absorbance spectrum, corresponding to the oscillations of free electrons along the particle's axial direction (longitudinal LSPR, L-LSPR) and orthogonal to the axis (transverse LSPR, T-LSPR). Charge density is comparatively lower in the L-LSPR mode, whereas it is higher in the T-LSPR mode. The restoring force exerted on the oscillating charges exhibits a proportional relationship with the accumulated charge, leading to a slower electron oscillation frequency in the L-LSPR mode (and thus a longer resonance wavelength) and a faster frequency in the T-LSPR mode (resulting in a shorter resonance wavelength).[36] At an azimuth angle of 0°, solely the L-LSPR mode is observed, with an absorption efficiency of 36.78 at a resonance wavelength of 1058 nm. At 90°, exclusively the T-LSPR mode is detected, but its contribution is negligible. At azimuth angles of 30° and 60°, both L-LSPR and T-LSPR modes are observed, and the resonance peaks remain

nearly unaltered. This phenomenon arises from the constant nanoparticle size and charge density. Irrespective of variations in particle dimensions, the T-LSPR wavelength is restricted to a narrow visible spectral range, whereas the L-LSPR wavelength can be tuned across a broad spectrum spanning from the visible to the NIR region. Furthermore, the intensity of the L-LSPR is significantly higher than that of the T-LSPR.

Synthesis and characterization of Au NRs@PEG

The simulation results indicated that Au NRs with a length of approximately 88 nm and a diameter of 13 nm have a resonance wavelength of 1058 nm, close to the 1064 nm laser wavelength. In order to investigate the therapeutic potential of these Au NRs in cervical cancer, a conventional seed-mediated method was employed to synthesize Au NRs with an average length of 87 $\pm$ 6 nm, a width of 13 $\pm$ 2 nm, and an aspect ratio of 6.76 (see Fig. 2a and e). Absorption spectroscopy revealed that the maximum absorption peak of Au NRs is observed at 513 nm and 1028 nm (Fig. 2g black line).

Typically, CTAB is used in the seed growth method for Au NRs synthesis, serving as a stabilizer and protective agent, helping to control the shape and size of the nanorods. However, when Au NRs are used for PTT, the CTAB in the solution exhibits high toxicity, which can interfere with the treatment process and hinder the interaction between the Au NRs and biomolecules. To enhance the biocompatibility and stability of the Au NRs, we modified their surface with polyethylene glycol (SH-5000-PEG). The results showed that the dispersibility, size (average length of 87.84 $\pm$ 6.19 nm, width of 13.28 $\pm$ 1.41 nm), aspect ratio of 6.61, and morphology of the Au NRs remained largely unchanged after PEG modification (Fig. 2b and f). High-resolution transmission electron microscopy (HRTEM) images of both Au NRs and Au NRs@PEG confirmed that they were highly crystalline (Fig. 2c and d). FTIR spectroscopy further confirmed the successful PEG coating on the Au NRs, showing characteristic C–H and C–O–C bonds, indicating the presence of PEG (Fig. S1). Additionally, the zeta potential of Au NRs and Au NRs@PEG shifted from positive to negative, with stable properties over 7 days (Fig. S2). Furthermore, the T-LSPR mode absorption peak of the PEG-modified Au remained consistent, while the L-LSPR mode absorption peak experienced an 8 nm red shift (Fig. 2g, red line).

Photothermal properties of Au NRs@PEG

The present study aims to investigate the photothermal performance of Au NRs@PEG under NIR-II light excitation at 1064 nm. To this end, a laser power of 500 mW cm^{-2} was selected to evaluate the photothermal properties of Au NRs@PEG at different concentrations (12.5, 25, and 50 μg mL^{-1}) using an infrared camera. The results demonstrated that at a concentration of 25 μg mL^{-1}, the temperature of Au NRs@PEG increased to 56.7 °C within 10 minutes, while the temperature change of water was negligible (Fig. 3a). As illustrated in Fig. 3b, the photothermal performance of Au NRs@PEG in an aqueous solution at a constant concentration (25 μg mL^{-1}) is demonstrated under various laser power irradiations. As anticipated, under 1064 nm laser irradiation, Au NRs@PEG demonstrated a discernible, laser power-dependent elevation in temperature. The photothermal properties of the Au NRs@PEG demonstrated no discernible alteration following five laser on-off heating cycles, as illustrated in Fig. 3c. PCE is defined as the ability of NPs to convert laser energy into heat. Subsequent to a 10 minute period of laser irradiation, the laser was deactivated, and the cooling rate was documented at 30 second intervals to assess the rate of heat transfer from the NPs to the surrounding environment (see Fig. 3d). In comparison with other agents, such as GNR@Ag (28.8%), Au@Metal–Organic Framework (30.2%),[36,37] the Au NRs@PEG demonstrated a high PCE of 60.89% at 1064 nm (Fig. 3e and Table S1).

In vitro cytotoxicity and PTT effect

For evaluating the *in vitro* photothermal efficacy, we examined the impact of NIR-II light irradiation on cancer cell ablation. As demonstrated in Fig. 4a, in the absence of laser exposure, HeLa cells exposed to varying concentrations of Au NRs@PEG exhibited minimal impact on cell viability, with no significant differences observed even at the maximum concentration of 120 μg mL^{-1}. This finding serves to substantiate the enhanced biocompatibility of Au NRs@PEG. Conversely, following NIR-II light exposure, HeLa cells incubated with Au NRs@PEG experienced significant photothermally mediated cell death, which was concentration-dependent. It is noteworthy that approximately 80% of the cells were eradicated when the Au NRs@PEG concentration reached 120 μg mL^{-1}, following minutes of irradiation with a 1064 nm laser (400 mW cm^{-2}). As illustrated in Fig. 4b and c, significant variations in migration distances were observed among the control group, the laser-only treatment group, the Au NRs@PEG-only treatment group, and the Au NRs@PEG + 1064 nm laser treatment group. The Au NRs@PEG + 1064 nm laser group showed a significant inhibitory effect on HeLa cell migration.

A comparative analysis revealed a marked decline in the number of migrating cells among the experimental subjects, accompanied by significant alterations in their cellular morphology as observed under microscopic scrutiny. The findings indicate that the amalgamation of Au NRs@PEG and 1064 nm laser irradiation (phototherapy) exerts a pronounced inhibitory effect on both cell proliferation and migration, particularly in HeLa cells.

Subsequent exploration of the photothermal performance of Au NRs@PEG was conducted, with visualization achieved *via* a live/dead cell fluorescence staining assay. In this assay, Calcein-AM (which emits green fluorescence to label viable cells) and PI (red fluorescence for dead cells) were utilized. The presence of strong green fluorescence (excitation wavelength: 488 nm) was detected in HeLa cells treated with 50 and 100 μg mL^{-1} of Au NRs@PEG prior to NIR-II laser irradiation (Fig. 5a). Following a 10 minute exposure to NIR-II laser irradiation, HeLa cells treated with 50 and 100 μg mL^{-1} Au NRs@PEG exhibited significant red fluorescence (561 nm), suggesting cell death. In contrast, HeLa cells not treated with Au NRs@PEG, subjected to the same NIR-II irradiation for 10 minutes, exhibited strong

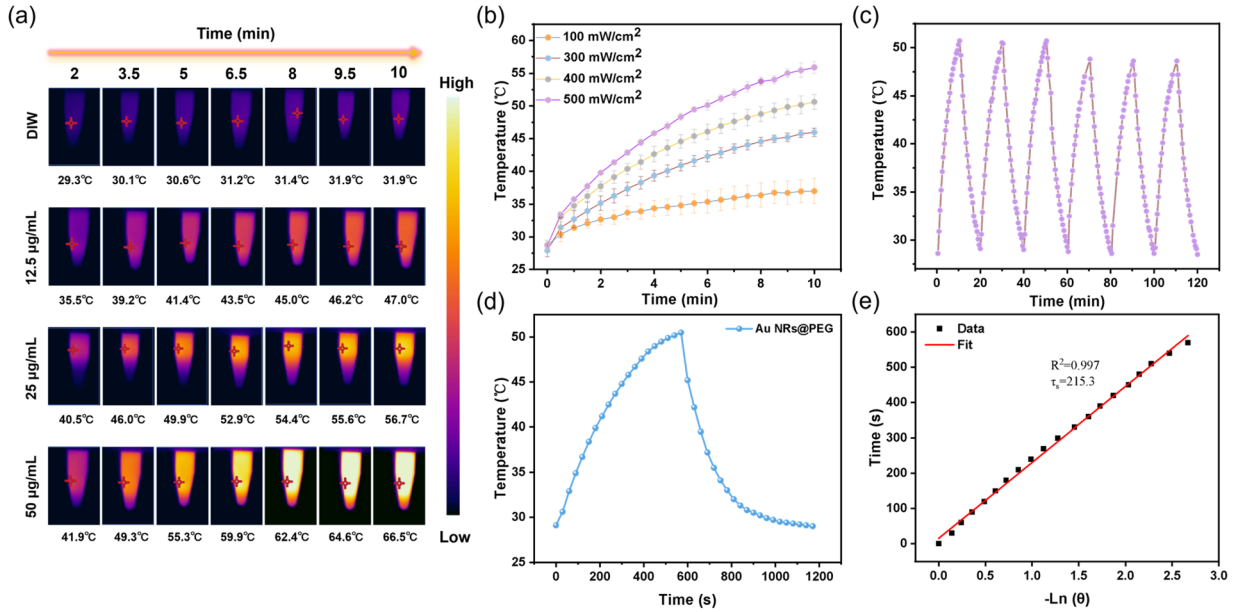

Fig. 3 *In vitro* evaluation of the photothermal performance of Au NRs@PEG. (a) Infrared thermographic images of Au NRs@PEG under 500 mW cm^{-2} laser exposure. (b) Temperature changes of 25 μg mL^{-1} Au NRs@PEG dispersions at 1064 nm under varying laser power densities. (c) Photothermal stability of Au NRs@PEG during continuous laser irradiation. (d) Heating and subsequent cooling curves of Au NRs@PEG throughout laser treatment. (e) Quantified PCE of Au NRs@PEG.

green fluorescence both before and after irradiation. This finding suggests that the laser did not directly induce cell death in the absence of Au NRs@PEG. In order to quantitatively evaluate the anticancer effectiveness of Au NRs@PEG, a flow cytometry analysis was performed on HeLa cells that had been labeled with PI and FITC after exposure to Au NRs@PEG. The

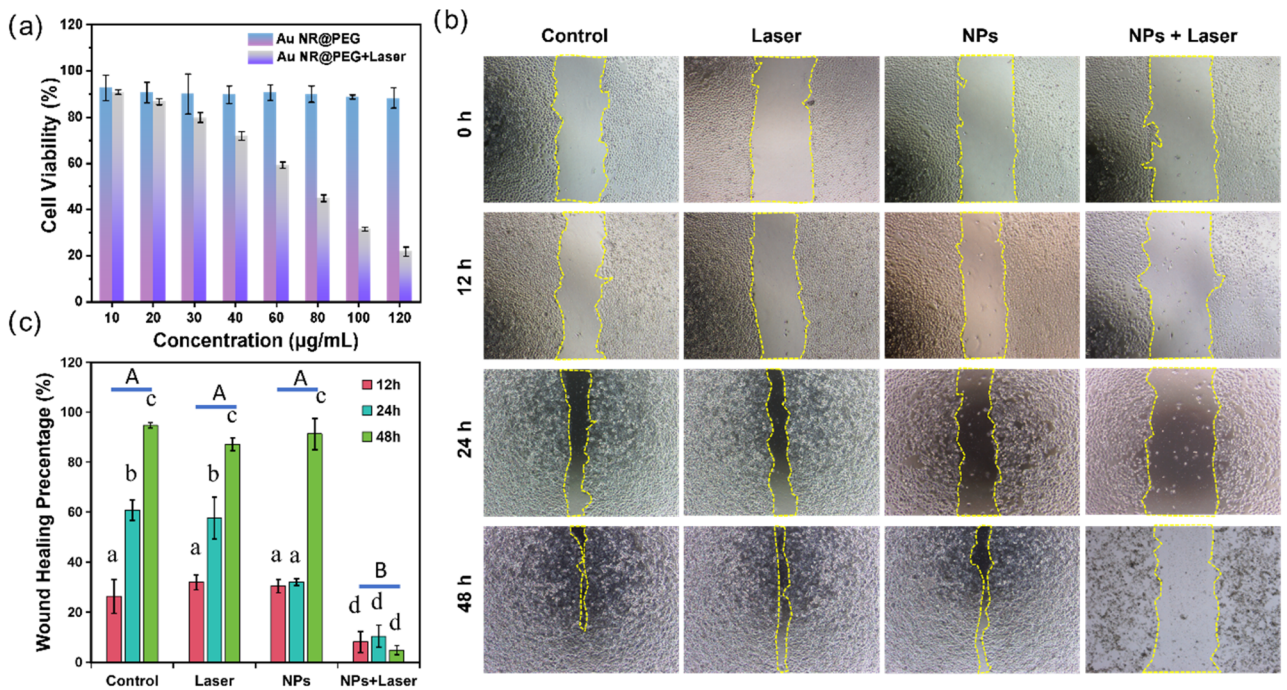

Fig. 4 *In vitro* applications of Au NRs@PEG. (a) Relative survival rate of CCK-8 cells under the action of Au-NR@PEG NPs. (b) The migratory inhibition of HeLa cells was assessed using a wound healing assay at 12, 24, and 48 hours. (c) The experiment was conducted in triplicate, with quantitative analysis performed using GraphPad software. Migration inhibition of HeLa cells was evaluated at 12, 24, and 48 hours using the wound healing assay. Each experiment was performed in triplicate, with quantitative data analysis conducted *via* GraphPad Prism. $^{**}p < 0.01$; $^{***}p < 0.001$.

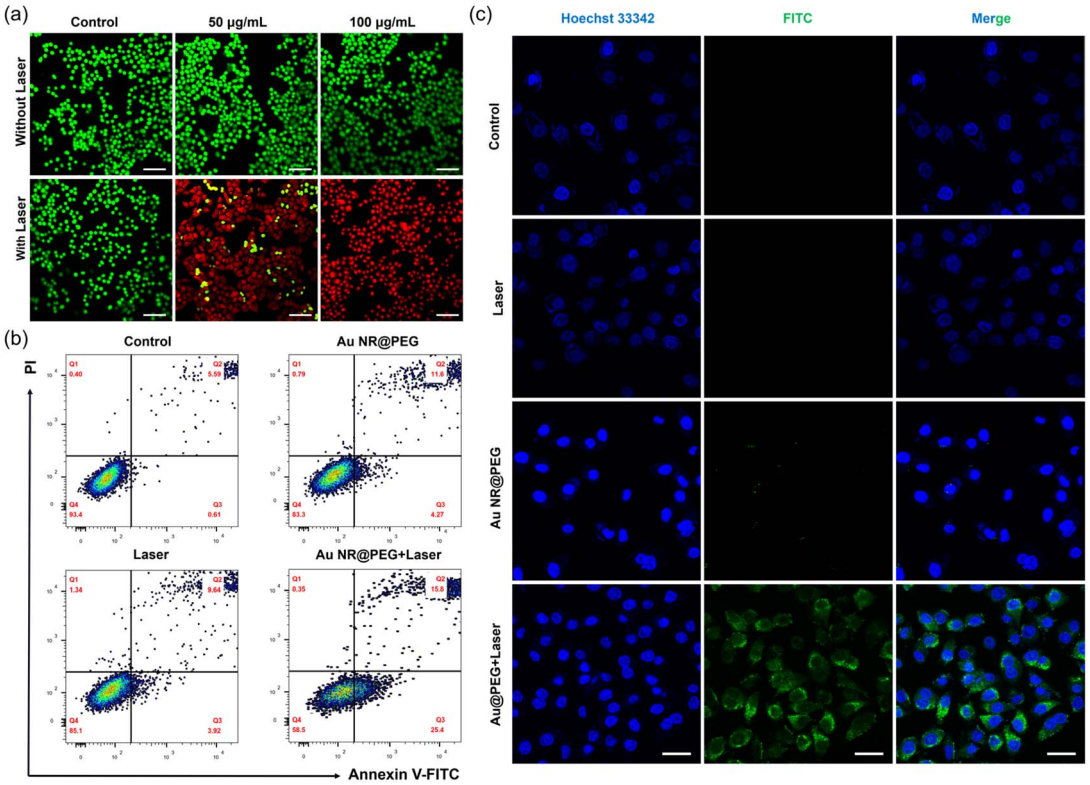

Fig. 5 Pro-apoptotic effect of Au NRs@PEG on tumor cells upon 1064 nm laser exposure. (a) Fluorescence images of the control group, 50 μg mL^{-1} and 100 μg mL^{-1} Au NRs@PEG groups, labeled with Calcein AM and PI prior to and following 1064 nm laser irradiation (1064 nm, 400 mW cm^{-2}, 10 min). (b) Flow cytometric analysis of apoptotic HeLa cells. (c) CLSM images of HeLa cells subjected to different treatment conditions (DMEM, 1064 nm laser alone, Au NRs@PEG alone, Au NRs@PEG + 1064 nm laser). Scale bar = 100 μm.

apoptosis rate in HeLa cells treated with Au NRs@PEG nanoparticles under 1064 nm laser irradiation significantly increased to 58.5% (Fig. 5b), confirming the photothermal-induced cell death. To further investigate the mechanism, we examined the changes in mitochondrial membrane potential. As shown in Fig. S3, HeLa cells treated with Au NRs@PEG and exposed to 1064 nm laser exhibited a noticeable decrease in mitochondrial membrane potential, evidenced by bright fluorescence signals, while other treatment groups did not show significant changes. This indicates mitochondrial damage under photothermal effects. Additionally, we assessed the expression of CRT and HMGB1 proteins in HeLa cells after various treatments. Only the Au NRs@PEG + laser-treated group showed externalization of CRT and release of HMGB1 (Fig. S4 and S5), indicating that the photothermal effect mediated by Au NRs@PEG under laser irradiation induces immunogenic cell death. These findings highlight that Au NRs@PEG, when exposed to 1064 nm laser irradiation, effectively promote apoptosis and enhance anticancer activity *via* photothermal effects.

In order to explore the therapeutic potential of Au NRs@PEG in PTT, the samples were observed *via* CLSM. The results demonstrated that HeLa cells labeled with FITC exhibited faint fluorescence signals in the absence of NIR-II irradiation. However, following exposure to NIR-II light, the fluorescence signals significantly intensified (Fig. 5c). These observations confirm that HeLa cells are effectively targeted and destroyed by the photothermal effects of Au NRs@PEG when combined with laser irradiation.

In vivo photothermal therapeutic effects and biosafety evaluation of Au NRs@PEG

It has been demonstrated that Au NRs@PEG, acting as a photothermal therapeutic agent, generates heat when exposed to laser irradiation, leading to the destruction of tumor cells, which is consistent with the findings of nanomaterials in cancer therapy.[38] To address biosafety and biodistribution concerns, we evaluated the *in vivo* fluorescence imaging and long-term biosafety of Au NRs@PEG. ICG was loaded onto the nanoparticles, and after intravenous injection into mice, NIR fluorescence imaging was performed at various time points. The results showed a rapid increase in liver fluorescence within the first 2 hours, peaking at 2 hours post-injection, followed by a gradual decrease and near-elimination by 48 hours. This indicates a short *in vivo* retention time, with clearance primarily *via* liver and kidney metabolism, reducing potential toxicity. These findings support Au NRs@PEG as a promising photothermal therapeutic agent for cervical cancer.

To further investigate its potential, we evaluated the *in vivo* photothermal therapeutic effects of Au NRs@PEG using animal models. The experimental procedure for *in vivo* treatment is

shown in Fig. 6a. For the *in vivo* evaluation, Au NRs@PEG was administered *via* intramuscular injection directly at the tumor site, and the temperature of the mice was continuously monitored with an infrared thermal imaging device. As demonstrated in Fig. 6b and c, during the 10 minute laser treatment, the temperature at the tumor site rapidly increased from approximately 34.5 °C to 50.5 °C, thereby substantiating that the photothermal effect of Au NRs@PEG generates sufficient heat to effectively treat tumors. In comparison, the control group exhibited a mere 3.4 °C rise in temperature after 10 minutes of laser irradiation, further substantiating the efficacy of Au NRs@PEG as a promising photothermal therapeutic agent for cervical cancer.

The *in vivo* anti-tumor activity of Au NRs@PEG was assessed using a cervical tumor-bearing mouse model. The experimental mice were separated into four distinct groups: a control group, a group that received laser treatment alone, a group that received Au NRs@PEG treatment alone, and a group that received a combination of laser and Au NRs@PEG treatment. A 1064 nm laser treatment was administered for a duration of 10 minutes, 12 hours subsequent to the injection of Au NRs@PEG. The results demonstrated no significant body weight reduction

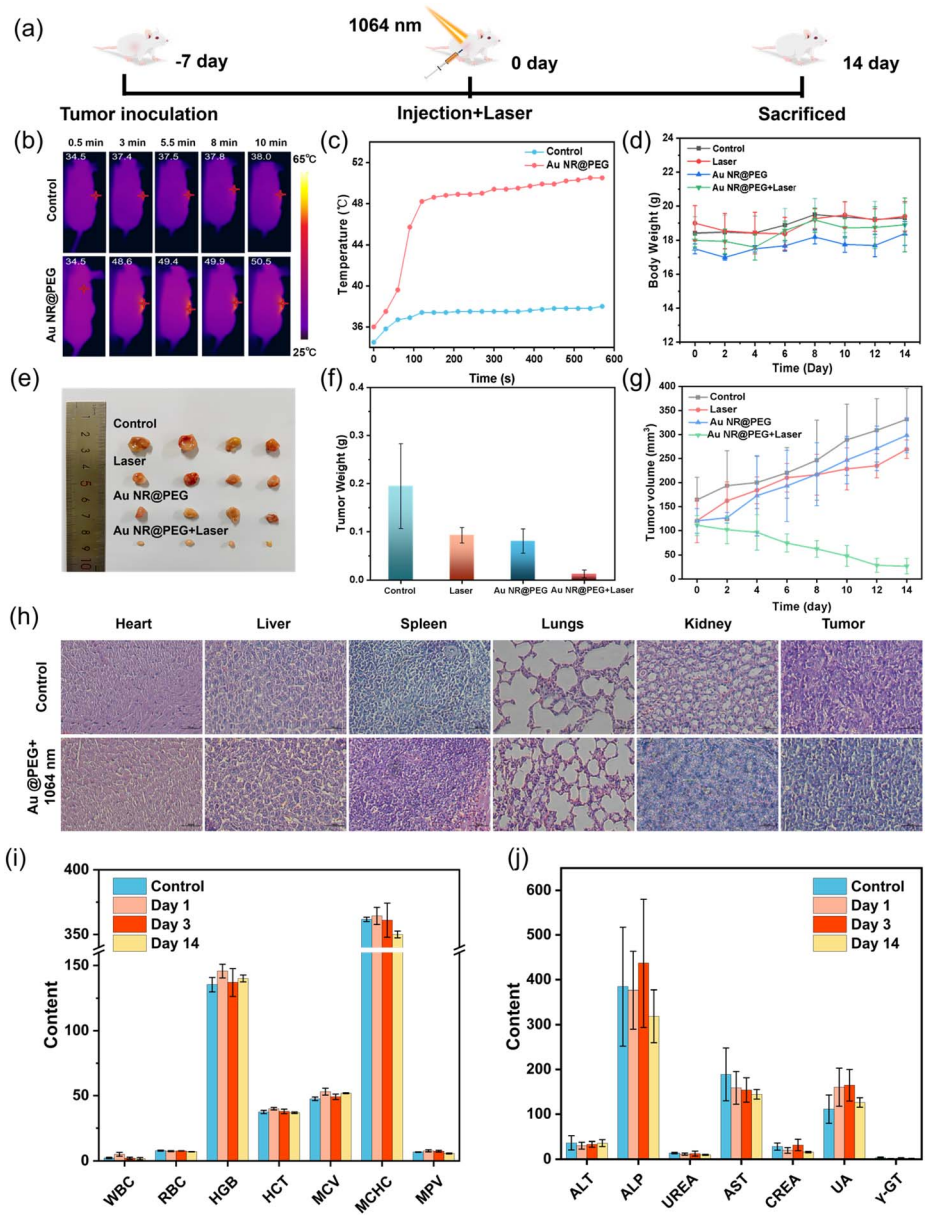

Fig. 6 *In vivo* PTT safety assessment. (a) Schematic of the *in vivo* therapeutic protocol. (b) Infrared thermographic images of HeLa tumor-bearing mice administered with PBS or Au NRs@PEG combined with 1064 nm laser (400 mW cm^{-2}), acquired at multiple time intervals. (c) Temporal temperature changes at the tumor site during laser exposure. (d) Body weight changes of mice during the treatment period. (e) Representative tumor images from the various treatment cohorts. (f) Tumor weights of each group 14 days after treatment. (g) Temporal changes in tumor volume over time. (h) H&E staining of tumors and organs isolated from mice in the control group and Au NRs@PEG + laser group. Scale bar = 50 μm for all images. (i and j) Hematological examinations and evaluations of liver and kidney function indicators.

following the PTT induced by small vesicles, indicating the absence of acute adverse effects from the treatment (Fig. 6d). As illustrated in Fig. 6e, f and g, during the 14 day monitoring period, the tumor volume in the control group exhibited a significant increase, as did the tumors in the Au NRs@PEG and 1064 nm laser groups. However, both tumor size and body weight in the Au NRs@PEG + 1064 nm laser-treated group demonstrated a decline. A significant reduction in tumor weight was observed in the Au NRs@PEG + 1064 nm laser-treated group after 14 days, with a tumor suppression rate of 93.5%, compared to the other groups.

At the conclusion of the monitoring period, the primary organs of mice were harvested, sectioned, and subjected to H&E staining. H&E revealed no substantial damage or necrosis in the tissue samples. The photothermal action of Au NRs@PEG successfully induced apoptosis in tumor cells, whereas the other treatments did not produce similar results, confirming the photothermal therapeutic efficacy.

Following irradiation with a 1064 nm laser, Au NRs@PEG induced apoptosis in tumor cells and inhibited tumor growth (Fig. 6h and S7). Additionally, no significant tissue or organ damage was observed after PTT, indicating that Au NRs@PEG does not harm major organs. Histological analysis of organs from treated tumor-bearing mice showed no adverse changes. Furthermore, hematological parameters were used to assess potential *in vivo* side effects on vital organs. Statistical analysis of all measured parameters in each treated cohort, compared to the control mice, revealed no significant differences (Fig. 6i and j), suggesting that the combined application of Au NRs@PEG and 1064 nm laser exposure does not negatively affect blood biochemical markers or liver and kidney functions. These results clearly demonstrate the excellent biological safety of Au NRs@PEG.

Conclusion

In summary, the light absorption properties of Au NRs were simulated numerically using the finite element method with a size-dependent refractive index model. The simulations indicated that Au NRs with a length of 88 nm and a diameter of 13 nm exhibited the highest PCE under NIR-II light irradiation. Based on these findings, we synthesized gold nanorods of the same dimensions (88 nm in length and 13 nm in diameter) using the seed-growth method and further functionalized them with PEG to enhance their stability and biocompatibility. The resulting Au NRs@PEG complex displayed an absorption peak at 1036 nm and demonstrated a high photothermal energy conversion efficiency of 60.89%. Moreover, Au NRs@PEG exhibited excellent photoacoustic signal generation and tissue penetration depth under 1064 nm irradiation. Both *in vitro* and *in vivo* experiments confirmed that Au NRs@PEG possess significant PTT efficacy and biosafety in the NIR-II spectral window. The nanoparticles have intrinsic optical properties that could enable imaging, and they demonstrate potential for future PTT applications.

Author contributions

Jiabao Xiong and Hairegu Tuxun: writing – original draft & editing. Jiayi Ding: software. Biao Dong and Nuernisha Alifu: writing – review & editing.

Conflicts of interest

There are no conflicts to declare.

Data availability

The authors confirm that the data supporting the findings of this study are available within the article.

Supplementary information (SI): a comparison of gold nanorods for therapeutic applications, FT-IR and zeta potential characterization of Au NRs@PEG, mitochondrial membrane potential analysis, CRT and HMGB1 immunofluorescence staining in HeLa cells, *in vivo* NIR-I fluorescence images and quantitative analysis, H&E staining of tumors and major organs, and additional references. See DOI: https://doi.org/10.1039/d5ra10095j.

Acknowledgements

This study received support from various funding agencies, including the State Key Laboratory of Pathogenesis Prevention and Treatment of High Incidence Disease and Central Asia, Xinjiang Medical University (No. SKL-HIDCA-2023-15), the Natural Science Foundation of Xinjiang Uygur Autonomous Region (No. 2022D01C727), the Talent Project of Tian Chi Doctoral Program in Xinjiang Uygur Autonomous Region (No. 0301050903), the Special Funds for Talents of Xinjiang Medical University (0103010211), the Key Scientific Research Program of Shaanxi Provincial Education Department (23JS016), the Natural Science Foundation of Xinjiang Uygur Autonomous Region (No. 2022D01C715), the College Students' Innovative Entrepreneurial Training Plan Program (X35), the Regional Collaborative Innovation Special Science and Technology Assistance Program of Xinjiang Uygur Autonomous Region (2022E02130), the Key Project (2022D01D40), the Outstanding Youth Project (2023D01E06), and the Youth Science Foundation (2022D01C215) of the Xinjiang Uygur Autonomous Region Natural Science Foundation. Additional support came from the National Natural Science Foundation of China (Grant No. 82073475, 62035011, 82260613, and 82060326). All animal procedures were performed in accordance with the Guidelines for Care and Use of Laboratory Animals of Xinjiang Medical University and approved by the Animal Ethics Committee of Xinjiang Medical University (IACUC-20230509-01).

References

1 X. Wang, L. Wang, S. Zong, R. Qiu and S. Liu, *Biomater. Sci.*, 2019, **7**, 3846–3854.
2 W. Small, M. A. Bacon, A. Bajaj, L. T. Chuang, B. J. Fisher, M. M. Harkenrider, A. Jhingran, H. C. Kitchener,

L. R. Mileshkin, A. N. Viswanathan and D. K. Gaffney, *Cancer*, 2017, **123**, 2404–2412.
3 R. S. Herbst, D. Morgensztern and C. Boshoff, *Nature*, 2018, **553**, 446–454.
4 X.-C. Zhang, J. Wang, G.-G. Shao, Q. Wang, X. Qu, B. Wang, C. Moy, Y. Fan, Z. Albertyn, X. Huang, J. Zhang, Y. Qiu, S. Platero, M. V. Lorenzi, E. Zudaire, J. Yang, Y. Cheng, L. Xu and Y.-L. Wu, *Nat. Commun.*, 2019, **10**, 1772.
5 O. Tacar, P. Sriamornsak and C. R. Dass, *J. Pharm. Pharmacol.*, 2013, **65**, 157–170.
6 D. Yoo, S. Jeong, H. M. Ju, W. Jeong, K. Kim and M.-J. Choi, *ACS Mater. Lett.*, 2024, **6**, 308–313.
7 K. M. Atkins, T. L. Chaunzwa, N. Lamba, D. S. Bitterman, B. Rawal, J. Bredfeldt, C. L. Williams, D. E. Kozono, E. H. Baldini, A. Nohria, U. Hoffmann, H. J. W. L. Aerts and R. H. Mak, *JAMA Oncol.*, 2021, **7**, 206–219.
8 G. Kothari, J. Korte, E. J. Lehrer, N. G. Zaorsky, S. Lazarakis, T. Kron, N. Hardcastle and S. Siva, *Radiother. Oncol.*, 2021, **155**, 188–203.
9 M. Xu, B. Xue, Y. Wang, D. Wang, D. Gao, S. Yang, Q. Zhao, C. Zhou, S. Ruan and Z. Yuan, *Small*, 2021, **17**, e2101397.
10 J. Nam, S. Son, K. S. Park, W. Zou, L. D. Shea and J. J. Moon, *Nat. Rev. Mater.*, 2019, **4**, 398–414.
11 X. Zhang, J. Tang, C. Li, Y. Lu, L. Cheng and J. Liu, *Bioact. Mater.*, 2021, **6**, 472–489.
12 M. Yang, J. Li, P. Gu and X. Fan, *Bioact. Mater.*, 2021, **6**, 1973–1987.
13 J. Conde, N. Oliva, Y. Zhang and N. Artzi, *Nat. Mater.*, 2016, **15**, 1128–1138.
14 Z. Chen, P. Zhao, Z. Luo, M. Zheng, H. Tian, P. Gong, G. Gao, H. Pan, L. Liu, A. Ma, H. Cui, Y. Ma and L. Cai, *ACS Nano*, 2016, **10**, 10049–10057.
15 A. N. Juaim, J. Sun, R. Nie, W. Li, L. Ding, K. Wang, J. Zhou, M. Li, M. Chi, B. Dong, M. Qi and L. Wang, *Small*, 2025, **21**, 2500382.
16 S. Li, Q. Deng, Y. Zhang, X. Li, G. Wen, X. Cui, Y. Wan, Y. Huang, J. Chen, Z. Liu, L. Wang and C. Lee, *Adv. Mater.*, 2020, **32**, 2001146.
17 Y. Tang and G. Wang, *J. Photochem. Photobiol., C*, 2021, **47**, 100420.
18 A. R. Rastinehad, H. Anastos, E. Wajswol, J. S. Winoker, J. P. Sfakianos, S. K. Doppalapudi, M. R. Carrick, C. J. Knauer, B. Taouli, S. C. Lewis, A. K. Tewari, J. A. Schwartz, S. E. Canfield, A. K. George, J. L. West and N. J. Halas, *Proc. Natl. Acad. Sci. U. S. A.*, 2019, **116**, 18590–18596.
19 R. Huang, C. Zhang, Y. Bu, Z. Li, X. Zheng, S. Qiu, J. O. Machuki, L. Zhang, Y. Yang, K. Guo and F. Gao, *Biomaterials*, 2021, **277**, 121088.
20 A. Sani, C. Cao and D. Cui, *Biochem. Biophys. Rep.*, 2021, **26**, 100991.
21 W. Yang, H. Liang, S. Ma, D. Wang and J. Huang, *Sustainable Mater. Technol.*, 2019, **22**, e00109.
22 S. Hwang, J. Nam, S. Jung, J. Song, H. Doh and S. Kim, *Nanomedicine*, 2014, **9**, 2003–2022.
23 K. Bandyopadhyay, S. Singh, V. K. Chaturvadi, A. K. Singh and A. Verma, *J. Mater. Chem. B*, 2025, **13**, 9720–9744.
24 J. Chen, X. Li, X. Zhao, Q. Wu, H. Zhu, Z. Mao and C. Gao, *Bioact. Mater.*, 2018, **3**, 347–354.
25 J. Song, X. Yang, O. Jacobson, P. Huang, X. Sun, L. Lin, X. Yan, G. Niu, Q. Ma and X. Chen, *Adv. Mater.*, 2015, **27**, 4910–4917.
26 X. Mi, Y. Wang, R. Li, M. Sun, Z. Zhang and H. Zheng, *Nanophotonics*, 2019, **8**, 487–493.
27 J. Zhao, A. O. Pinchuk, J. M. McMahon, S. Li, L. K. Ausman, A. L. Atkinson and G. C. Schatz, *Acc. Chem. Res.*, 2008, **41**, 1710–1720.
28 V. Myroshnychenko, J. Rodríguez-Fernández, I. Pastoriza-Santos, A. M. Funston, C. Novo, P. Mulvaney, L. M. Liz-Marzán and F. J. García de Abajo, *Chem. Soc. Rev.*, 2008, **37**, 1792–1805.
29 A. Amirjani and S. K. Sadrnezhaad, *J. Mater. Chem. C*, 2021, **9**, 9791–9819.
30 X. Song and J. Li, *Plasmonics*, 2023, **18**, 661–676.
31 K. M. McPeak, S. V. Jayanti, S. J. P. Kress, S. Meyer, S. Iotti, A. Rossinelli and D. J. Norris, *ACS Photonics*, 2015, **2**, 326–333.
32 A. D. Rakić, A. B. Djurišić, J. M. Elazar and M. L. Majewski, *Appl. Opt.*, 1998, **37**, 5271.
33 A. Moroz, *J. Opt. Soc. Am. B*, 2011, **28**, 1130.
34 H. Yang, H. Huang, X. Ma, Y. Zhang, X. Yang, M. Yu, Z. Sun, C. Li, F. Wu and Q. Wang, *Adv. Mater.*, 2021, **33**, 2103953.
35 M. A. Garcia, *J. Phys. D: Appl. Phys.*, 2011, **44**, 283001.
36 Z. Mei, D. Gao, D. Hu, H. Zhou, T. Ma, L. Huang, X. Liu, R. Zheng, H. Zheng, P. Zhao, J. Zhou and Z. Sheng, *Biomaterials*, 2020, **251**, 120092.
37 X. Deng, S. Liang, X. Cai, S. Huang, Z. Cheng, Y. Shi, M. Pang, P. Ma and J. Lin, *Nano Lett.*, 2019, **19**, 6772–6780.
38 A. D. Tripathi, Y. Labh, S. Katiyar, A. K. Singh, V. K. Chaturvedi and A. Mishra, *ACS Appl. Bio Mater.*, 2024, **7**, 7838–7851.